Dust acoustic wave properties in varying discharge volumes

C. A. Knapek ✉ iD ; M. Schwabe iD ; V. Yaroshenko; P. Huber iD ; D. P. Mohr iD ; U. Konopka

Check for updates

CHORUS

View Online

Export Citation

Dust acoustic wave properties in varying discharge volumes

C. A. Knapek,[1,2,a)] (ID) M. Schwabe,[2,3] (ID) V. Yaroshenko,[2,4] P. Huber,[2] (ID) D. P. Mohr,[1,2,3] (ID) and U. Konopka[5]

AFFILIATIONS

[1]Institute of Physics, University of Greifswald, 17489 Greifswald, Germany
[2]Institut für Materialphysik im Weltraum, Deutsches Zentrum für Luft- und Raumfahrt, 51147 Köln, Germany
[3]Deutsches Zentrum für Luft- und Raumfahrt (DLR), Institut für Physik der Atmosphäre, 82234 Oberpfaffenhofen, Germany
[4]Institut für Solar-Terrestrische Physik, Deutsches Zentrum für Luft- und Raumfahrt, 17235 Neustrelitz, Germany
[5]Physics Department, Auburn University, Auburn, Alabama 36849, USA

[a)]Author to whom correspondence should be addressed: christina.knapek@physik.uni-greifswald.de

ABSTRACT

Properties of self-excited dust acoustic waves under the influence of active compression of the dust particle system were experimentally studied in the laboratory and under microgravity conditions (parabolic flight). Ground based laboratory experiments clearly show that wave properties can be manipulated by changing the discharge volume, its aspect ratio, and thus the dust particle density. Complementary experiments under microgravity conditions, performed to exclude the effects of gravity inflicted sedimentation and anisotropic behavior, were less conclusive due to residual fluctuations in the planes acceleration indicating the need for a better microgravity environment. A theoretical model, using plasma parameters obtained from particle-in-cell simulations as input, supports the experimental findings. It shows that the waves can be described as a new observation of the dust acoustic mode, which demonstrates their generic character.

I. INTRODUCTION

Complex or dusty plasmas consist of nano- or microparticles embedded in a low temperature plasma. The microparticles get highly charged by collecting ions and electrons from the surrounding plasma. They interact with each other via a screened Coulomb potential.[1] In astrophysical environments, dusty plasma occurs, for instance, in the rings surrounding Saturn,[2] above the lunar surface,[3,4] in the vicinity of comets,[5] and in interstellar clouds.[6] Dusty plasmas are intensively studied also in laboratory surroundings, where the individual components (dust, ions, and electrons) can be more easily controlled, and their individual contribution to the dynamics and structure can be examined. For example, an ion flow through a cloud of suspended microparticles can induce an ion streaming instability and lead to the formation of dust acoustic waves (DAW), also referred to as dust density waves (DDW).[7] These are waves that are visible in the microparticle fluid as zones of compression and rarefaction which travel in the direction of ion flow—in ground experiments, this is typically downward, since the microparticles are suspended in or near the sheath region of the plasma where the force

of gravity is compensated by strong electric fields. To reduce the effect of gravity on the microparticles, experiments are often performed in microgravity, either on board the International Space Station or[8–11] during parabolic flights,[12–14] or by compensating gravity by some other methods such as gas flow or thermophoresis.[15,16] Despite the fact that ions move more slowly in the plasma bulk than in the sheath region, waves are also observed under microgravity conditions provided that the number density of particles is large enough. In that case, the waves typically are symmetric around a particle-free central region, the so-called void, which is produced due to the balance of electrostatic and ion drag force in the plasma bulk. Figure 1(a) shows the typical appearance of waves under microgravity conditions. The wave fronts are visible as higher density/brighter regions in concentric ellipses surrounding the void. They move outward from the void toward the electrodes, which are located outside the field of view in the top and bottom of the image.

Often, the condition for the excitation of dust acoustic waves is given in terms of the local electric field E being larger than a critical electric field E_{cr},[15]
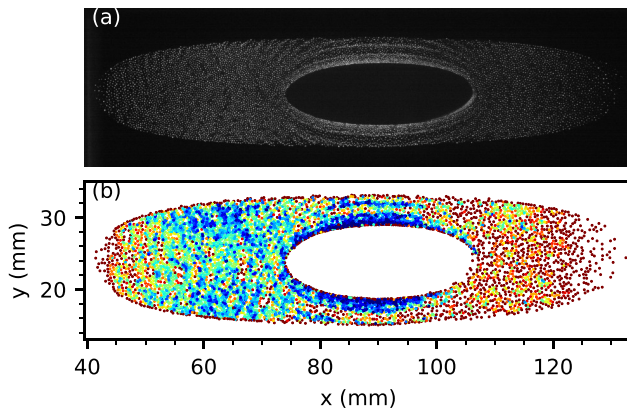
FIG. 1. (a) Image of a dusty plasma under "microgravity" conditions, showing the typical "void" structure as well as concentric crests of a self-excited dust wave. The image corresponds to the instant of time between regions I and II shown in the periodgram in Fig. 3(a). (b) Detected particle positions color coded by the area of the surrounding Voronoi cells varying between 0.05 mm² or smaller (black) and 0.25 mm² or larger (red). The vertical position y is given in mm above the bottom electrode.

$$E \geq E_{\mathrm{cr}} = \frac{\nu_{dn}}{C}\frac{k_B T_i}{|e|}, \quad (1)$$

where ν_{dn} denotes Epstein's gas damping coefficient,[17] k_B is the Boltzmann's constant, T_i is the ion temperature, e is the electron charge, and $C = \omega_{\mathrm{pd}}\lambda_D$ is the dust acoustic speed, with the microparticles' plasma frequency ω_{pd} and the effective Debye length λ_D.[7] Also note that Eq. (1) is only valid for a limited range of microparticle and ion collisionalities.[18]

The dependence of the excitation conditions on the number density of the microparticles is contained in Eq. (1) via the dust acoustic speed respectively the microparticle plasma frequency—the larger the number density n_d, the larger ω_{pd}, the larger C, and thus the smaller the critical electric field that has to be overcome. Recent experimental and theoretical works have shown that the Havnes parameter may be a key factor in the excitation of the wave modes[19]—this parameter $\mathcal{H} = Z_d n_d / n_i$ gives the ratio between the microparticle charge density, expressed in terms of the microparticle charge number Z_d and density n_d, to the ion charge density, expressed with the ion number density n_i.

In the present study, we investigate this dependence further by experimentally compressing a microparticle cloud, thus instantaneously changing the particle density. The experiments were performed on ground and in the microgravity phase of a parabolic flight. The results are supported by theoretical considerations. In the following, the term dust acoustic wave will be used to emphasize the theoretical interpretation of the observed wave behavior.

The paper is organized as follows: In Sec. II A, we describe the experimental setup used for both experiments. The experimental parameters and data analysis methods are given in Secs. II B and II C, followed by a summary of the results in Sec. II D. Section III introduces a theoretical model for the observed waves. The theory uses plasma parameters obtained from plasma simulations described in Sec. III A. The paper is concluded in Sec. IV.

II. EXPERIMENTS

A. Experimental setup

The experiments presented in this paper were performed in the Zyflex chamber,[20,21] which is a versatile radio frequency (RF) plasma chamber, a prototype developed for a future complex plasma research facility on board the International Space Station (ISS). The chamber offers the unique capability to change the distance between its electrodes on-the-fly during experimental runs. Figure 2 shows a sketch of the chamber and supporting hardware. The parallel electrode bodies in the Zyflex chamber each accommodate a central disk electrode with a diameter of 80 mm, and a surrounding ring electrode with an outer diameter of 120 mm. A four-channel RF generator drives each electrode segment independently at the usual frequency of 13.56 MHz. By design, the electrode distance can be varied between 25 and 75 mm, with ring and center electrodes on one side being permanently linked. In the currently operated prototype, smaller separations down to ≈20 mm are possible, too. The electrode bodies are surrounded by grounded guard rings shielding the plasma in the center from the chamber walls. The guard rings can be moved independently from the electrodes. In the experiments presented in this paper, guard rings and electrode bodies were kept at the same level on each side. Details on the chamber's capabilities can be found elsewhere.[21] Three microparticle dispensers are mounted into the side walls of the chamber and allow injection of the large amount of microparticles necessary to fill the chamber volume. A vertically (between the electrodes) spread and horizontally focused laser illuminates a central plane perpendicular to the electrodes in the chamber, and cameras record the motion of the microparticles inside this laser plane.

B. Parabolic flight experiments

In order to test the dependence of wave properties on the number density of the microparticles, we performed a series of experiments during the 35th DLR Parabolic Flight Campaign in 2020. In these experiments, particles were injected into the chamber after the start of the microgravity phase, and once a large cloud formed, the electrode distance was varied.

A common occurrence during a parabolic flight is an observable drift of the central particle-free void out of the field of view—most likely caused by systematic accelerations along the flight direction due to the flight maneuver itself, which are evident in the residual acceleration measurements. Since the effect of this drift on the local excitation conditions for waves is not yet understood, in the following we focus on two distinct parabolas in which there were periods of time during which the visible size of the void was relatively stable.

During the two selected parabolas, argon at a pressure of 10 Pa was used as the background gas. Spherical melamine-formaldehyde (MF) microparticles with a diameter of 9.19 μm were injected into the plasma after the microgravity phase started. For the first run, the peak-to-peak voltage on all electrode segments (center and ring) was initially set to 50 V. Shortly after particle injection, the power to the ring segments was switched off. This decreases the extent of the bulk plasma and confines the particle cloud to a smaller volume in the chamber center, thus further increasing the particle density. Subsequently, the electrode separation was increased from 32.5 to 34.6 mm. In the second run, the voltage on the center segments was set to 40 V, with no power to the ring segments. The electrode distance was then decreased
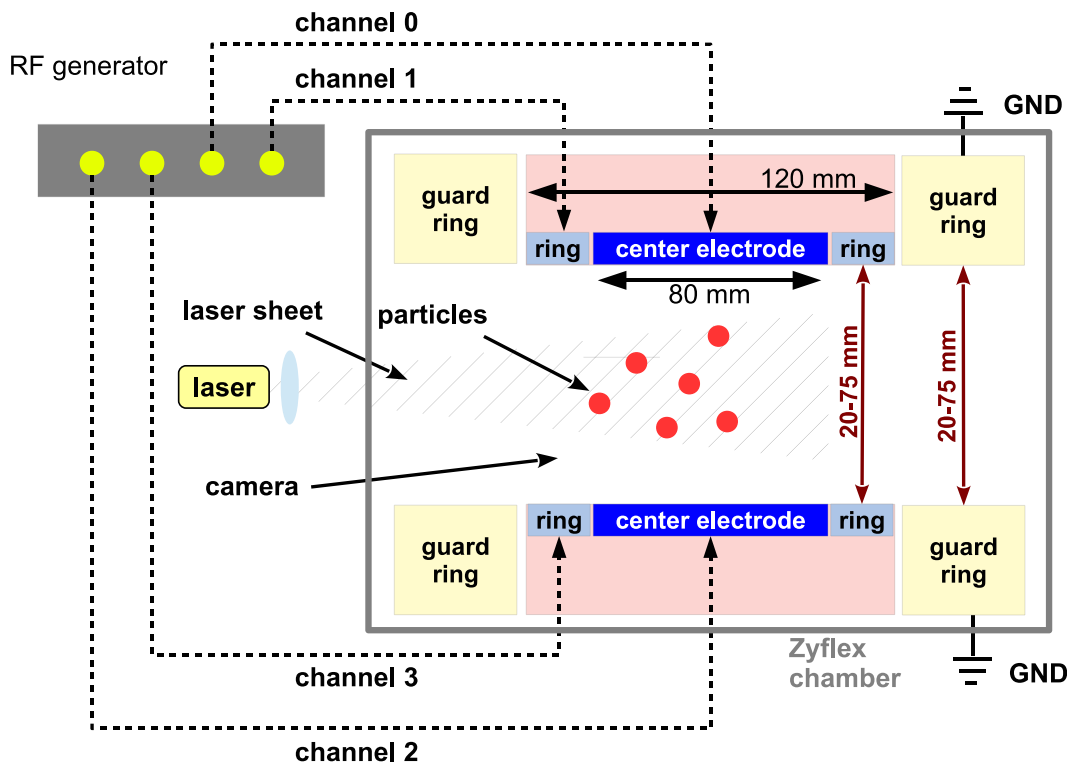
FIG. 2. Sketch of the Zyflex chamber as a 2D cross section, and supporting hardware. The chamber has two parallel electrode bodies (red) each holding a central disk electrode and a ring electrode. The electrode bodies are surrounded by grounded guard rings (yellow). Electrode bodies, as well as the guard rings, can be moved independently in vertical direction to adjust the plasma volume. A four-channel RF generator drives the electrode segments independently. Particles are injected from dispensers mounted in the chamber side walls. They are illuminated by a vertically extended laser sheet, and images of the scattered light are recorded by video cameras.

from 36.7 to 31.8 mm. Experimental parameters are also summarized in Table I.

Figure 1 shows the particle cloud [experiment Flight (aI) in Table I] as seen with the overview camera at one instant of time. The waves traveling outward from the void are clearly visible in the original image [Fig. 1(a)]. In order to determine the local density, we found the particle positions in the images using the moment method[23] and then calculated the Voronoi cell surrounding each particle [see Fig. 1(b)]. The cell area A is a measure that corresponds to the "2D number density" of the microparticles and can be converted into the 3D number density by

$$n_d = \frac{1}{d \cdot A} \qquad (2)$$

using the horizontal focus width of the laser sheet of $d \approx 140\,\mu$m in the center of the chamber, where the measurements of wave properties were performed. Histograms of the Voronoi areas A yield an average area for each measurement that is determined by the position of the maximum peak of the histogram for the respective regime. The areas given in Table I correspond to the position of that peak. In the following, the particle density will be expressed by the Voronoi areas A derived from the data. It is noted that to obtain (real) three-dimensional particle densities, a 3D optical diagnostic (e.g., a stereoscopic system[24]) or fast scanning of the 2D diagnostics through the particle cloud would be necessary, both of which are not implemented in the current setup.

Figure 3 shows time–space plots (periodgram)[25] calculated by summing up the central 8.3 mm wide region of each original image in the time sequence in the horizontal direction and stacking all resulting line plots next to each other. The brighter the periodgrams, the higher the microparticle density at that location.[22] Dust density wave fronts are visible in these periodgrams as brighter, periodically occurring diagonal stripes.

We selected two and three regions for further analysis, marked in Figs. 3(a) and 3(b), respectively, with Roman numerals and white vertical lines. In these regions, we manually counted the occurrence of wave fronts along the time direction (the horizontal axis in the image) to obtain the wave frequency, and we measured the distance to the next wave front along the spatial direction (the vertical axis in the image) to obtain the wavelength. The results are given in Table I, from which it can be noted that the wavelength decreases with decreasing electrode distance and increasing particle density $\propto 1/A$. The method of manual analysis of the waves was chosen due to the small size of the regions where the waves appear, and due to the noisy data, which made it difficult to reliably apply a Fourier transformation.

C. Ground experiments

We performed complementary experiments in the ground laboratory by compressing particle clouds containing waves. Figure 4 shows the side view of the particle cloud as the electrodes were moved

TABLE I. Experimental parameters and measured wave parameters for the different experimental runs. The particle diameter is denoted by d_d, the distance between the electrodes by ΔL, the height of the considered area with waves above the bottom electrode by h, the measured area of the Voronoi cells (proportional to the inverse of the number density n_d) by A, the wavelength with λ, and the wave frequency with f. Note that the quality of the particle tracking at small electrode distances is diminished due to the increased particle density (decrease in particle separation) and subsequent reduction in the reliability of particle identification. The experiments were performed at 10 Pa in argon.

Experiment	d_d (μm)	ΔL (mm)	h (mm)	A (mm^2)	λ (mm)	f (Hz)
Flight (aI)	9.19	32.5	7.5–9.5	0.068	1.3	8.4
Flight (aII)	9.19	32.5 → 34.6	7.2–12.5	0.078 → 0.135	1.7 → 2.4	7.1
Flight (bI)	9.19	36.7 → 35.1	21.9–27.1	0.157 → 0.160	1.9 → 2.0	5.1
Flight (bII)	9.19	33.9 → 32.7	7.9–13.4	0.183 → 0.178	1.6 → 1.5	4.5
Flight (bIII)	9.19	32.7 → 31.8	7.6–12.6	0.139 → 0.153	1.4 → 2.1	5.0
Ground (a)	1.31	66.2	18.1–34.6	0.080	2.4	∼19
Ground (b)	1.31	61.0	17.9–31.4	0.072	2.1	∼21.5
Ground (c)	1.31	55.1	17.7–29.6	0.060	1.8	14.8, ∼25
Ground (d)	1.31	51.4	17.4–30.8	0.055	1.7	14.3, 15.4, ∼27
Ground (e)	1.31	47.7	17.0–29.1	0.049	1.7	16.0, ∼26
Ground (f)	1.31	43.9	15.8–26.5	0.046	1.5	14.1, 15.6
Ground (g)	1.31	40.1	14.7–23.6	0.040	1.6	14.8
Ground (h)	1.31	36.2	13.4–20.3	0.038	1.4	15.4
Ground (i)	1.31	32.6	12.4–17.1	0.036	1.1	18.4
Ground (j)	1.31	29.3	10.6–15.5	0.036	1.1	15.9, 22.2
Ground (k)	1.31	25.5	9.2–13.5	0.035	1.3	17.9, 25.0
Ground (l)	1.31	21.4	7.8–11.3	0.039	1.5	16.8

together. The experiment was performed in argon with a gas flow rate of 400 msccm at a pressure of 10 Pa. The gas flow was led through a shower-head at the outer edge of the guard-rings, ensuring that disturbances of the particles due to gas flow are minimized. The peak-to-peak voltage on the top central disk electrode was 44 V, on the top ring electrode 30.5 V, on the bottom disk electrode 19.5 V, and on the bottom ring electrode 16 V as measured with an oscilloscope. This asymmetric configuration ensured a vertically large cloud extent against gravity. Spherical MF particles with a diameter of 1.31 μm and mass density of 1.51 g/cm^3 made up the microparticle cloud. The same particles were kept in the chamber during the experiment, and no new particles were added. The electrode distance was gradually decreased from 66.2 to 21.4 mm (see also Table I), and for each step, we recorded time series of images with fixed electrode distances. During the last recording at an electrode distance of 21.4 mm, filaments were observed in the plasma glow indicating the onset of plasma instabilities.

For the ground dataset, the same analysis steps as for the parabolic flight data were performed: The particle positions were found by tracking via the moment method, and a Voronoi analysis yielded the cell areas A as a measure for the local particle density.

We again calculated periodograms from the time series of particle images, see Figs. 5(a) and 5(b) for two examples at different electrode separations. In the original images, a region of less bright, less dense particles below the main cloud is visible. We assume that these are agglomerates that are levitated below the main cloud due to their higher mass. In the following analysis, we concentrate on the main
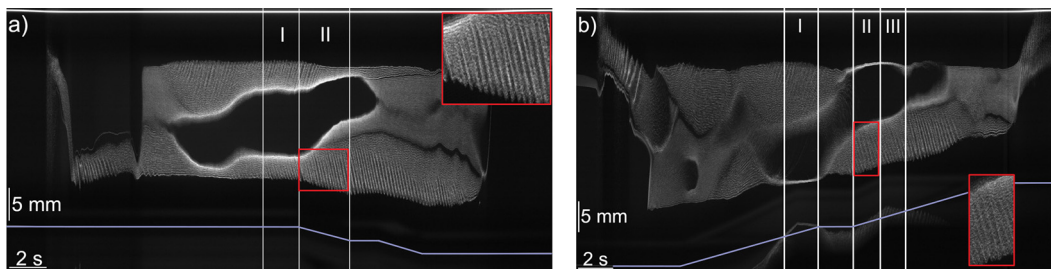

FIG. 3. Space–time plots (periodograms) of the particle clouds during two parabolas, denoted Flight aI–II (a) and bI–III (b) in Table I. The periodograms are produced by summing up the central 8.3 mm wide region of each original image in the time sequence in horizontal direction and stacking all resulting line plots next to each other. In these images, the pixel brightness is proportional to the particle number density.[22] Here, the direction of gravity before and after the parabolas is up due to the orientation of the cameras. The central void can be seen as empty region in the middle of the images. Wave crests are visible as diagonal bright stripes. The Roman numerals I–III mark the analyzed regions. The blue solid lines indicate the position of the moving electrode (the other electrode was held fixed at the position of the horizontal solid white line visible in the top of the images). Note that in (b) the reflections of particles in the lower image part are reflections off the guard ring, not the electrode.
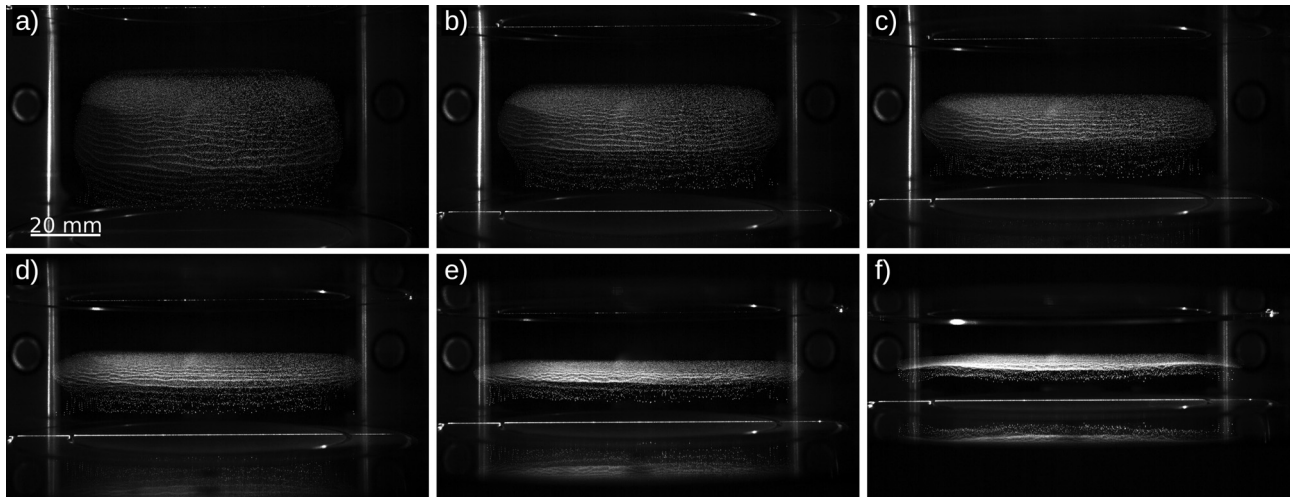
FIG. 4. Original (contrast and brightness enhanced) side views of the particle cloud and electrodes during the ground experiments (letters correspond to experiment labels in Table I). The top and bottom electrodes are visible as horizontal stripes. The electrode distances ΔL were (a) $\Delta L = 66.2$, (b) $\Delta L = 55.1$, (c) $\Delta L = 47.7$, (d) $\Delta L = 40.1$, (e) $\Delta L = 32.6$, and (f) $\Delta L = 25.5$ mm. In the latter recordings, a reflection of the particle cloud on the bottom electrode becomes visible.

cloud of particles. In order to find the wavelengths of the waves, we cut a horizontal slab from that part of the periodgram corresponding to the bottom region of the main cloud. This slab had a height of 765 μm and spanned the entire width of the periodgram, that is, the
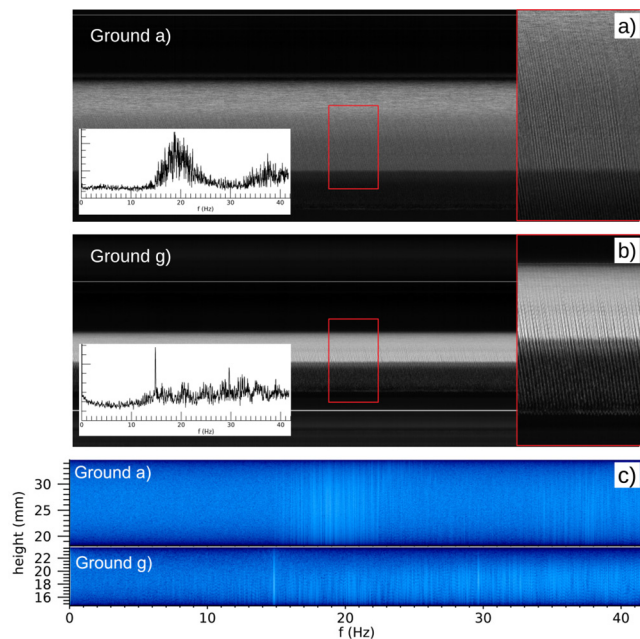
FIG. 5. (a) and (b) periodgrams of datasets "ground (a)" and "ground (g)." The insets on the right enlarge a region to make the wave structure more visible. (c) Spectra obtained by Fourier transforming the periodgrams along the time domain for dataset "ground (a)" (top) and "ground (g)" (bottom). The vertical axes show the position above the bottom electrode. The respective vertically summed-up spectra are shown as insets on the left in (a) and (b).

entire time of the recorded time series. Then, we shifted this slab upward by one pixel and calculated the correlation between the shifted slab and the original periodgram. When the slab had reached the position of the next wave ridge, the correlation had a peak, and the distance that the slab was shifted to reach that peak corresponded to the wavelength.

In order to obtain the wave frequencies, we cut the periodgrams to the bright regions without agglomerates and performed Fast Fourier Transforms along the time dimension. Figure 5 shows two exemplary resulting spectra. For the largest electrode distance, the spectrum was broad without any dominant peaks. At more narrow electrode separations, peaks appeared at various frequencies between 14 and 18 Hz (see Fig. 5 for two examples of spectra and Table I for all determined frequencies). There was no clear dependence of the frequency on the electrode distance. In Table I, we give a range of frequencies for broad spectra such as those shown in Fig. 5 (top) and the exact location of the peak for spectra such as those shown in Fig. 5 (bottom).

D. Results

Figure 6 (top) shows the measured wavelengths as a function of the inverse of the area of the Voronoi cells, which is proportional to the microparticle number density. Figure 6 (bottom) shows the dependence of the wavelengths on the electrode distance. It can be seen that in general, for the ground experiments (red crosses), the wavelength increases with rising electrode distance and falling microparticle density. At the smallest electrode separations (runs k and l), an increase in the wavelength can be observed [Fig. 6(b)]. In these cases, the particle density in the region of the waves shows a slight decrease in contrast to the density increase with increasing compression for the runs a–j. The density decrease could be attributed to a larger horizontal extent of the cloud (visible in Fig. 4). Another possibility is the loss of particles dropping out of the plasma outside of the field of view. Due to the particle density decrease, the wavelengths at the smallest electrode
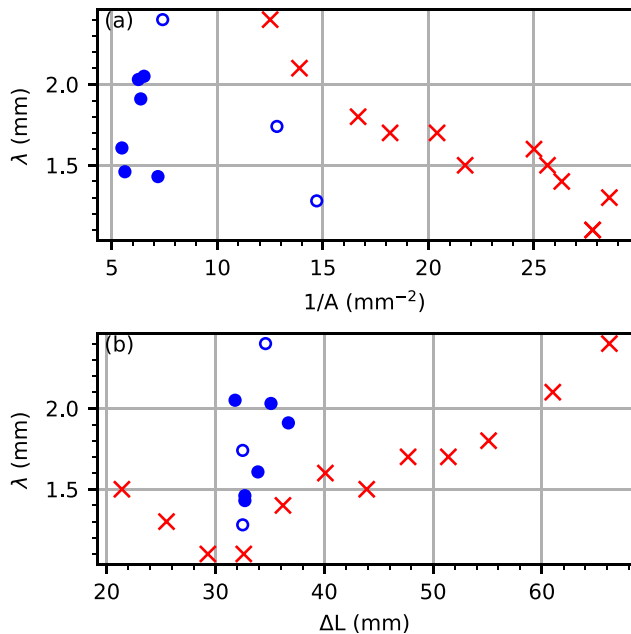
FIG. 6. Dependence of the measured wavelength λ on (a) the inverse of the area A of the Voronoi cells, which is proportional to the microparticle number density, and (b) the electrode distance ΔL for the datasets "Flight (aI)-(aII)" (blue empty) and "Flight (bI)-(aIII)" (blue filled circles), and the ground experiment (red crosses). Error bars for the ground data are of the size of the plot symbols (the uncertainty of λ is defined by the shift of the slab in the correlation analysis by 1 px = 0.0765 mm). For the flight experiments (blue symbols), both the minimum and maximum wavelengths given in Table I are represented by separate circles.

separations are of the order of those at a larger distance of 36.2 mm (run h) with comparable particle density. For the microgravity experiments, the dependence can be seen only very weakly for experiment run Flight (a) (open blue circles), while in run Flight (b) (filled blue circles), the measured wavelengths do not seem to depend on the microparticle density. One problem of parabolic flights as a platform for such investigations is the short time of microgravity in general (≈ 22 s) and its quality. The residual gravitational forces (jitter) induce fluctuations in the particle system, and further, there are acceleration forces due to the flight maneuver along the plane's axis in the flight direction that cause a motion of the whole particle cloud, as explained in the beginning of Sec. II B. During the experiments performed on ground, the particle system was compressed and then left alone to stabilize for several seconds, which was not possible in the short time provided by the parabola, and would have been hindered by the present fluctuations. Also, the electrode separation could not be changed over a large range, again due to the short time. Therefore, the microgravity results cannot reproduce the behavior of the ground experiments, but they at least indicate that the compression and density increase in general can be achieved and, given a more stable platform (e.g., the ISS), should produce valuable results in the future.

In Sec. III, a theoretical model is developed that supports the selected method of wave property manipulation and characterizes the detected waves as dust acoustic waves.

III. THEORETICAL CONSIDERATIONS

First, we introduce the main parameters, which govern the dispersion relation and the instability threshold in the considered experiments. The ion thermal Mach number is $M_i = u_i/V_{Ti}$, where u_i stands for the ion flow velocity and $V_{Ti} = \sqrt{T_i/m_i}$ is the ion thermal velocity (T_i and m_i denote the ion temperature and mass, respectively). The ion (i) and particle (d) collisionality parameters are defined through $\theta_\alpha = \nu_{\alpha n}/\omega_{p\alpha}$ with appropriate indices $\alpha = i, d$, notations $\omega_{p\alpha}$ and $\nu_{\alpha n}$ stand for the ion/dust plasma frequency, and ion/dust-neutral collision frequencies, respectively.

A. Simulations

In order to characterize these parameters quantitatively, we employ the results of particle-in-cell (PIC) simulations performed for the Zyflex chamber in the particle-free argon plasma at the pressure 10 Pa and various distances between electrodes $\Delta L = 25, 50, 75$ mm.

The simulations were performed with xoopic, a 2D3V PIC code,[26] for a 2D cross section through the center of the plasma chamber, yielding 2D distributions of superparticles of electrons and ions (each superparticle consisting of 2×10^6 physical particles), and the respective velocities in 3D. Additionally, the electric field and plasma potential are obtained. All values are spatially coarse grained on a grid with the cell size of 1 mm in each direction in the 2D plane. The time step between iterations was 1×10^{-11} s for the electron distribution, while the distribution of the slower ions was evaluated for each 20th time step.

Simulations provide variations of the plasma density n_0, electron temperature T_e, and vertical distribution of the electric field $E(y)$. It turns out that the dependence of n_0 and T_e on ΔL can be rather well described by simple linear fits: $n_0 \simeq (0.4 + 0.268\Delta L(\text{mm})) \times 10^7$ (cm^{-3}) and $T_e \simeq (4.93 - 0.0367\Delta L(\text{mm}))$ (eV), where the electrode separation ΔL is expressed in mm. In our further modeling, the calculated plasma number density n_0 is associated with the ion density n_i, i.e., $n_0 \simeq n_i$ (as it would be in the absence of negatively charged particles). The ion temperature is assumed to be close to room temperature $T_i \simeq 0.025$ eV. The electric field predicted by the PIC simulations changes significantly at different electrode separations as well as inside the particle cloud, when ΔL is fixed. In the latter case, $E(y)$ can vary from values $E(y) \sim 1$ V/cm at the upper part of the dust cloud ($y \simeq y_2$) to $E(y) \sim 10$ V/cm at the bottom part ($y \simeq y_1$), close to the sheath.

B. Theory

To deal with wide variations of the predicted plasma parameters and electric fields, we have calculated the charges acquired by the particles in two limiting cases. The first case mimics the bulk plasma conditions in the upper part of the dust cloud and corresponds to the subthermal ions $M_i \lesssim 1$, while the second case relates to the superthermal ion flows $M_i > 1$ and may be relevant for the bottom part of the particle cloud. Note that in the latter case, the respective thermal Mach number has been calculated by substitution of the highest electric field $E(y) \simeq E(y_1)$ in a modified Frost formula.[27] Figure 7 shows the resulting particle charge numbers Z_d as functions of the electrode separation. In both cases, the standard OML (orbital motion limited) theory has been modified to incorporate a finite particle density, n_d [see Eq. (2) and data in Table I]. For the subthermal case, we also took into

08 April 2024 14:36:46
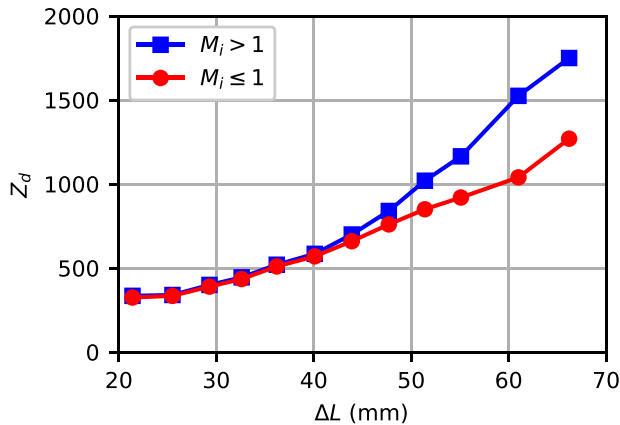
FIG. 7. Charge number Z_d as a function of electrode separation ΔL (mm) for particle radius: $a = 0.65\,\mu$ m calculated for the plasma and particle parameters near the upper ($M_i \lesssim 1$) and lower ($M_i > 1$) boundary of the region where the waves were excited.

account an increase in the ion flux to the particle surface due to the weakly collisional regime of the ions.[28,29] Both curves in Fig. 7 indicate a strong reduction (by a factor of $\sim 4 - 5$) of the particle charge which tends to be $Z_d \simeq n_i/n_d$ at high plasma compression. Finally, this effect provides a decreasing dust plasma frequency $\omega_{pd} = \sqrt{4\pi e^2 Z_d^2 n_d/m_d}$ with a reduction in ΔL (here m_d denotes the particle mass).

Using the standard Epstein drag formula,[30] one can evaluate the particle–neutral collisional frequency ν_{dn} and hence the critical electric field E_{cr} given by Eq. (1). Figure 8 displays the respective critical ion Mach number M_{cr} providing the onset of the ion flow instability as a function of the electrode separation. The variations of the quantity M_{cr} have been calculated using the particle charges prescribed by the lower curve in Fig. 7. For comparison, we also display in Fig. 8 variations of
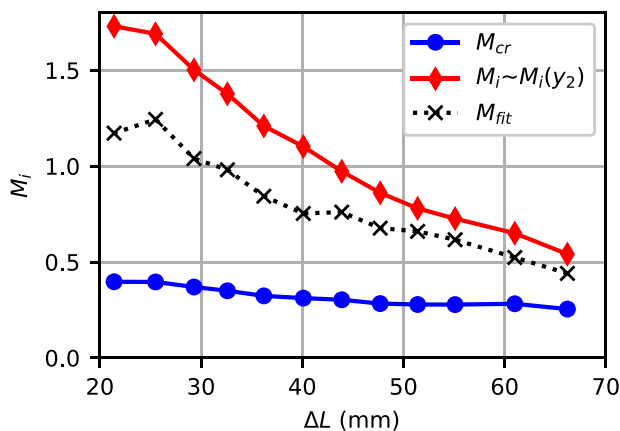

FIG. 8. Ion Mach number M_{cr} (blue dots) corresponding to the critical field, Eq. (1), and ion Mach number $M_i \sim M_i(y_2)$ (red diamonds) following from the electric field providing the balance of the electric and gravitational forces [close to numerical estimations of $E(y_2)$] as a function of the distance between the electrodes in the ground experiments. The ion Mach number M_{fit} (black crosses) obtained from a fit of the theoretical model to the experimentally obtained wave numbers is shown, as described in the text below.

the ion Mach number M_i based on the estimations of the electric field providing the levitation of the particles $E \simeq gm_d/eZ_d$ that appear very close to the numbers given by PIC simulations in the upper part of the particle cloud $E(y_2)$. It is seen that M_{cr} values are of the same order of magnitude at the large separation distance $\Delta L \gtrsim 45$ mm, but may be a few times less than the respective numerical estimates of $M_i(y_2)$ for more compressed plasmas ($\Delta L < 45$ mm). Note that the electric field in the bottom part of the cloud is larger, which leads to an increase in the Mach number (increased drift velocity). While this can lead to an increased phase velocity for the waves in the bottom part of the cloud,[16] the periodograms (Fig. 5) indicate that in the presented experiments the change of the wave velocity is not significant. A possible explanation could be the simultaneous decrease in particle charge in the bottom cloud, which would in turn decrease the dust plasma frequency and thus the wave speed.

For future experiments in microgravity, where particles are located in the plasma bulk, variations of the electric field are expected to be much smaller.

We assume that the excitation of the dust density waves occurs for the electric field $E \gtrsim E_{cr}$, so that the ion drift in the region of the wave excitation is close to the subthermal ($M_i \lesssim 1$). Employing the particle charges corresponding to the subthermal regime (the lower curve in Fig. 7), and measured particle density, one can estimate the plasma frequency ω_{pd} and the respective collisionality parameter θ_d. Furthermore, we calculate the ion–neutral collision frequency in argon gas ν_{in} using an approximation accounting for the ion drift[31] $M_i \lesssim 1$, and thus get the ion collisionality parameter θ_i. In Fig. 9, we plot variations of the collisionality parameters θ_i and θ_d vs the electrode separation ΔL. Although both curves θ_i and θ_d grow when ΔL decreases, the particle component remains collisionless or weakly collisional ($\theta_d < 1$) even in the most compressed case, but ions become collisional $\theta_i \lesssim 1$, especially at strong plasma compression.

Using the obtained parameter regime, we calculate the dispersion relations at different ΔL and compare the results with the corresponding experimental data. Following the general scheme, the waves will be described by the electrostatic dispersion relation that in terms of the plasma susceptibilities can be written as
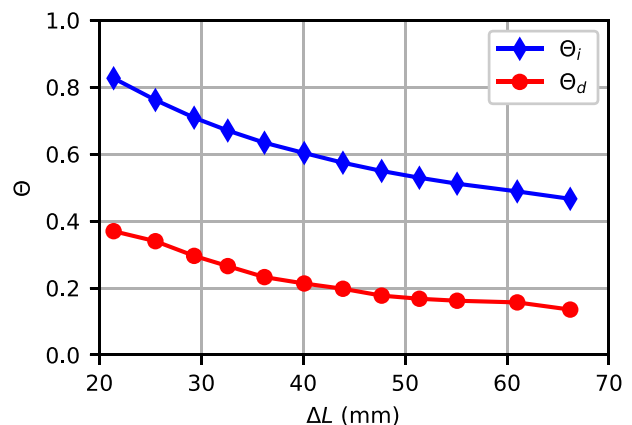
FIG. 9. Variations of the collisionality parameters for ions $\theta_i = \nu_{in}/\omega_{pi}$ and particles $\theta_d = \nu_{dn}/\omega_{pd}$, vs the electrode separation ΔL (mm). Calculations are done for the case $M_i \lesssim 1$.

$$\tilde{\omega} = \frac{\omega}{\omega_{pd}} = -i\frac{\theta_d}{2} + \left(-\frac{\theta_d^2}{4} + \frac{1}{1 + \chi_e + \chi_i} \right)^{1/2}. \qquad (3)$$

The susceptibility of the electrons is given in a standard way by $\chi_e = 1/k^2\lambda_{De}^2$, where k and λ_{De} are the wave number and the electron Debye length. In the case of subthermal ion drift and ion collisional regime, the ion susceptibility can be derived from a fluid model.[18] This leads to

$$\chi_i \simeq \frac{1}{ix M_i \theta_i + x^2(1 - M_i^2)}. \qquad (4)$$

Here, the small wave frequency has been neglected compared to the term ku_i for typical ion flow velocities and ion collision frequencies. The normalized wavenumber is given by $x = k\lambda_{Di}$.

To model the situation in the interior of the particle cloud, the experimentally obtained wave numbers were used as input for the wave dispersion relation, Eq. (3), to find the ion Mach numbers that fit best the experimental data. The procedure was to identify, via a root search of the derivative of $Im(\tilde{\omega})$, the value of M_i for a given x for which the imaginary part of Eq. (3) has its maximum. The found M_{fit}, presented in Fig. 8 as black crosses, lie between the critical ion Mach number and the Mach number corresponding to the electric field providing the balance of the electric and gravitational forces, thus confirming the theoretical model and chosen parameters. The ion and particle collisionality parameters were introduced in Fig. 9. Figure 10 presents three examples of the dispersion relations (3) of the low-frequency mode propagating along the ion flow for three different ΔL and respective M_{fit}, θ_i, and θ_d. Solid (dashed) curves represent the real and imaginary parts of the normalized wave frequency $Re(\tilde{\omega})$ and $Im(\tilde{\omega})$ as functions of the normalized wavenumber x. The dispersion relations show an increase in the frequency $Re(\tilde{\omega})$ with wave number, which is asymptotically linear at small wave numbers and resembles a shape of standard dust–acoustic dispersion $Re(\tilde{\omega}) = x/\sqrt{1 + x^2}$ shown by dotted curve in Fig. 10. The growth rate which is determined
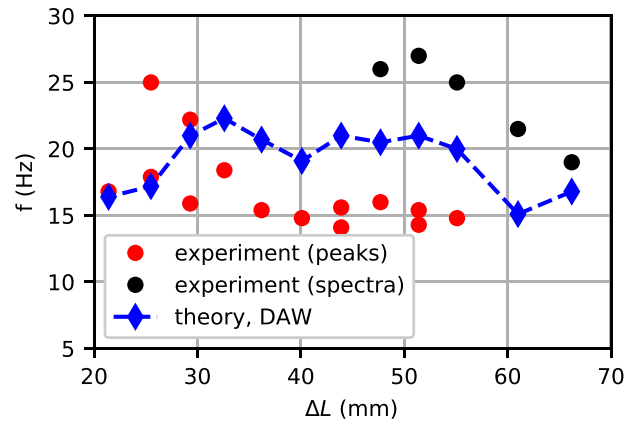
FIG. 11. Comparison of the measured wave frequencies (red circles: frequency peaks and black circles: broader spectra) with frequencies corresponding to the standard dust acoustic wave (diamonds) at different plasma compressions.

by the positive value of $Im(\tilde{\omega})$ increases for smaller electrode separation. The fastest growing mode which finally has to determine the observed wave in the experiments corresponds to the maximum of $Im(\tilde{\omega})$. It is seen that the theoretical wave frequency at the position corresponding to the maximum of the growth rate (defined by the experimentally obtained wavenumber, crosses in Fig. 10) appears close to the respective experimental wave characteristics. Hence, the calculated dispersion curves approach the experimental situation for considered ΔL displaying a good quantitative agreement. This finding supports the correct choice of the plasma and particle parameters, which determine the wave dispersion. The wave frequencies obtained from the experimental data (see Table I) are shown in Fig. 11 for different electrode separations, divided into the observed distinct peaks and broad spectra. In the latter case, the central wavelength of the spectra was taken. The frequency does not exhibit a visible dependence on the electrode separation. A possible explanation is described as follows: The increase in the particle charge with increasing electrode separation yields an increase in the dust plasma frequency and thus the dust acoustic speed. At the same time, the Mach number decreases with increasing electrode separation due to a decrease in the ion drift speed. In the simplified picture of the long wavelength limit, the contributions of both effects cancel each other out and a nearly constant frequency is obtained for the observed parameter range.

Finally, we have calculated variations of the dust acoustic frequency $\omega = \omega_{pd} x/\sqrt{1 + x^2}$ at various distances between electrodes and compare them to the respective measured values (shown by circles in Fig. 11). One finds a reasonable quantitative agreement. Therefore, the theoretical result consistent with the experimental findings indicates that at various electrode separations, the wave propagates rather as a standard dust acoustic wave in the direction of the electric field. In summary, the density waves detected under different plasma compressions in the Zyflex chamber can be considered as a new observation of the dust acoustic mode, which demonstrates its generic character.

IV. CONCLUSIONS

We presented experimental observations of self-excited dust-acoustic waves in a complex plasma under gravity conditions as well as in a microgravity environment (parabolic flight). During the
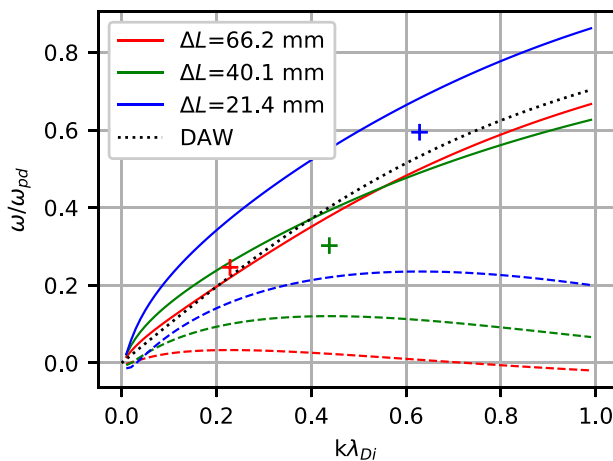

FIG. 10. Real (solid) and imaginary (dashed) part of the wave frequency normalized to the particle plasma frequency vs normalized wavenumber $x = k\lambda_{Di}$ for various electrode separations ΔL, calculated for Mach numbers M_{fit}. The respective experimentally measured wave characteristics are indicated by crosses.

08 April 2024 14:36:46

experiments, the wave properties were actively changed by varying the distance between the electrodes of the rf discharge chamber, thereby compressing the particle system and thus increasing the particle density. The experiments yield wavelengths and frequencies of the excited modes. In the ground experiments, where particles are vertically confined in an extended plasma sheath region, it could be observed that with increasing density, the wavelength becomes smaller. The wave frequency is more or less unaffected, though at large electrode separations (small densities), no distinct peaks can be found in the frequency spectra. Instead, here a broader spectrum in the vicinity of the peaks for higher density is found. Apparently, no distinct wave modes are excited in this case. The experiments performed in microgravity, where particles were located in the plasma bulk region, do not reproduce this behavior. One problem is the rather unstable situation during parabolic flights, where the residual gravity fluctuations disturb the particle cloud, and the experiment time is limited to 22 s, which does not allow a large compression factor due to the limits of the electrode motion speed.

A theoretical model confirms that the observed waves are indeed DAWs, and a quantitative agreement between theory and experiments can be found. The theory used plasma parameters T_e, n_e and the estimated electric fields that were obtained from PIC simulations. The estimated particles charges decrease with decreasing electrode separation (increasing particle density), while the ion Mach number and collisionality parameters increase due to the change in the electric field during the plasma compression. Ion Mach numbers that match the observed wave properties were identified by fitting the model to the experimentally measured wavenumbers, and a quantitative agreement was found. This confirms the validity of theoretical model and chosen simulation results.

In conclusion, the compression of the particle cloud is an effective tool to study DAWs. To shed more light on the dependence of the waves on particle densities and the critical electric field, future experiments require a stable microgravity environment such as on the ISS. Especially, the wave properties in particle systems located in the plasma bulk rather than those in the plasma sheath region (where the electric field is usually larger than E_{crit}) could be investigated in such an environment. Employing appropriately designed hardware that includes options for an additional manipulation of the electric fields independent of the plasma compression, as is planned for the future complex plasma facility COMPACT on board the ISS, would allow to study the onset of the self-excited waves and the respective conditions.

ACKNOWLEDGMENTS

AUTHOR DECLARATIONS

Conflict of Interest

The authors have no conflicts to disclose.

Author Contributions

Christina A. Knapek: Conceptualization (equal); Formal analysis (equal); Investigation (equal); Project administration (lead); Visualization (equal); Writing – original draft (equal). **Mierk Schwabe:** Conceptualization (equal); Formal analysis (equal); Investigation (equal); Visualization (equal); Writing – original draft (equal). **Victoria V. Yaroshenko:** Formal analysis (equal); Visualization (equal); Writing – original draft (equal). **Peter Huber:** Data curation (supporting); Investigation (equal); Software (supporting); Writing – review & editing (equal). **Daniel Paul Mohr:** Data curation (lead); Investigation (equal); Software (lead); Writing – review & editing (equal). **Uwe Konopka:** Conceptualization (equal); Investigation (equal); Writing – review & editing (equal).

DATA AVAILABILITY

The data that support the findings of this study are available from the corresponding author upon reasonable request.

REFERENCES

[1] A. Melzer, *Physics of Dusty Plasmas* (Springer, 2019), Vol. 962.

[2] G. E. Morfill and H. M. Thomas, "Spoke formation under moving plasma clouds—The Goertz-Morfill model revisited," Icarus **179**, 539 542 (2005).

[3] E. Grün, M. Horanyi, and Z. Sternovsky, "The lunar dust environment," Planet. Space Sci. **59**, 1672 1680 (2011).

[4] S. K. Mishra, "Nonlinear dust acoustic perturbations within dusty plasma over sunlit lunar surface," Phys. Plasmas **28**, 033702 (2021).

[5] H. Chen, W. Yang, and S. Liu, "Dust-ion-acoustic modes at comet 67P/Churyumov-Gerasimenko," Phys. Plasmas **26**, 112104 (2019).

[6] A. V. Ivlev, A. Burkert, A. Vasyunin, and P. Caselli, "Compact dusty clouds and efficient H_2 formation in diffuse interstellar medium," Astrophys. J. **861**, 30 (2018).

[7] R. L. Merlino, "25 years of dust acoustic waves," J. Plasma Phys. **80**, 773 (2014).

[8] H. M. Thomas, G. E. Morfill, V. E. Fortov, A. V. Ivlev, V. I. Molotkov, A. M. Lipaev, T. Hagl, H. Rothermel, S. A. Khrapak, R. K. Sütterlin, M. Rubin-Zuzic, O. F. Petrov, V. I. Tokarev, and S. K. Krikalev, "Complex plasma laboratory PK-3 plus on the international space station," New J. Phys. **10**, 033036 (2008).

[9] M. Y. Pustylnik, M. A. Fink, V. Nosenko, T. Antonova, T. Hagl, H. M. Thomas, A. V. Zobnin, A. M. Lipaev, A. D. Usachev, V. I. Molotkov, O. F. Petrov, V. E. Fortov, C. Rau, C. Deysenroth, S. Albrecht, M. Kretschmer, M. H. Thoma, G. E. Morfill, R. Seurig, A. Stettner, V. A. Alyamovskaya, A. Orr, E. Kufner, E. G. Lavrenko, G. I. Padalka, E. O. Serova, A. M. Samokutyayev, and S. Christoforetti, "Plasmakristall-4: New complex (dusty) plasma laboratory on board the international space station," Rev. Sci. Instrum. **87**, 093505 (2016).

[10] L. Yang, M. Schwabe, S. Zhdanov, H. M. Thomas, A. M. Lipaev, V. I. Molotkov, V. E. Fortov, J. Zhang, and C.-R. Du, "Density waves at the interface of a binary complex plasma," Europhys. Lett. **117**, 25001 (2017).

[11] J. Goree, B. Liu, M. Y. Pustylnik, H. M. Thomas, V. E. Fortov, A. M. Lipaev, V. I. Molotkov, A. D. Usachev, O. F. Petrov, M. H. Thoma, E. Thomas, U. Konopka, and S. Prokopiev, "Correlation and spectrum of dust acoustic waves in a radio-frequency plasma using PK-4 on the international space station," Phys. Plasmas **27**, 123701 (2020).

[12] M. Himpel, T. Bockwoldt, C. Killer, K. O. Menzel, A. Piel, and A. Melzer, "Stereoscopy of dust density waves under microgravity: Velocity distributions and phase-resolved single-particle analysis," Phys. Plasmas **21**, 033703 (2014).

[13] E. Zaehringer, M. Schwabe, S. Zhdanov, D. P. Mohr, C. A. Knapek, P. Huber, I. L. Semenov, and H. M. Thomas, "Interaction of a supersonic particle with a three-dimensional complex plasma," Phys. Plasmas **25**, 033703 (2018).

[14] S. Schütt, M. Himpel, and A. Melzer, "Experimental investigation of phase separation in binary dusty plasmas under microgravity," Phys. Rev. E **101**, 043213 (2020).

[15] M. A. Fink, S. K. Zhdanov, M. Schwabe, M. H. Thoma, H. Höfner, H. M. Thomas, and G. E. Morfill, "Autowaves in a dc complex plasma confined behind a Laval nozzle," Europhys. Lett. **102**, 45001 (2013).

[16] P. Bajaj, S. Khrapak, V. Yaroshenko, and M. Schwabe, "Spatial distribution of dust density wave properties in fluid complex plasmas," Phys. Rev. E **105**, 025202 (2022).

[17] P. S. Epstein, "Zur Theorie des Radiometers," Z. Phys. A **54**, 537–563 (1929).

[18] S. Khrapak and V. Yaroshenko, "Ion drift instability in a strongly coupled collisional complex plasma," Plasma Phys. Controlled Fusion **62**, 105006 (2020).

[19] V. V. Yaroshenko, S. A. Khrapak, M. Y. Pustylnik, H. M. Thomas, S. Jaiswal, A. M. Lipaev, A. D. Usachev, O. F. Petrov, and V. E. Fortov, "Excitation of low-frequency dust density waves in flowing complex plasmas," Phys. Plasmas **26**, 053702 (2019).

[20] C. A. Knapek, P. Huber, D. P. Mohr, E. Zaehringer, V. I. Molotkov, A. M. Lipaev, V. Naumkin, U. Konopka, H. M. Thomas, and V. E. Fortov, "Ekoplasma—Experiments with grid electrodes in microgravity," AIP Conf. Proc. **1925**, 020004 (2018).

[21] C. A. Knapek, U. Konopka, D. P. Mohr, P. Huber, A. M. Lipaev, and H. M. Thomas, "'Zyflex': Next generation plasma chamber for complex plasma research in space," Rev. Sci. Instrum. **92**, 103505 (2021).

[22] M. Schwabe, S. K. Zhdanov, H. M. Thomas, A. V. Ivlev, M. Rubin-Zuzic, G. E. Morfill, V. I. Molotkov, A. M. Lipaev, V. E. Fortov, and T. Reiter, "Nonlinear waves externally excited in a complex plasma under microgravity conditions," New J. Phys. **10**, 033037 (2008).

[23] D. Mohr, C. Knapek, P. Huber, and E. Zaehringer, "Algorithms for particle detection in complex plasmas," J. Imaging **5**, 30 (2019).

[24] A. Melzer, M. Himpel, C. Killer, and M. Mulsow, "Stereoscopic imaging of dusty plasmas," J. Plasma Phys. **82**, 615820102 (2016).

[25] M. Schwabe, M. Rubin-Zuzic, S. Zhdanov, H. M. Thomas, and G. E. Morfill, "Highly resolved self-excited density waves in a complex plasma," Phys. Rev. Lett. **99**, 095002 (2007).

[26] J. P. Verboncoeur, A. B. Langdon, and N. T. Gladd, "An object-oriented electromagnetic PIC code," Comput. Phys. Commun. **87**, 199–211 (1995).

[27] S. A. Khrapak and A. G. Khrapak, "Modified frost formula for the mobilities of positive ions in their parent gases," AIP Adv. **9**, 095008 (2019).

[28] M. Lampe, R. Goswami, Z. Sternovsky, S. Robertson, V. Gavrishchaka, G. Ganguli, and G. Joyce, "Trapped ion effect on shielding, current flow, and charging of a small object in a plasma," Phys. Plasmas **10**, 1500–1513 (2003).

[29] S. A. Khrapak, S. V. Ratynskaia, A. V. Zobnin, A. D. Usachev, V. V. Yaroshenko, M. H. Thoma, M. Kretschmer, H. Höfner, G. E. Morfill, O. F. Petrov, and V. E. Fortov, "Particle charge in the bulk of gas discharges," Phys. Rev. E **72**, 016406 (2005).

[30] P. S. Epstein, "On the resistance experienced by spheres in their motion through gases," Phys. Rev. **23**, 710–733 (1924).

[31] S. A. Khrapak, "Practical expression for an effective ion-neutral collision frequency in flowing plasmas of some noble gases," J. Plasma Phys. **79**, 1123–1124 (2013).

08 April 2024 14:36:46